

Effect of the Metallicity on the X-ray Emission from the Warm-Hot Intergalactic Medium

Ursino, E.¹, Galeazzi, M.¹, and Roncarelli, M.²

Physics Department, University of Miami, Coral Gables, FL 33155

Dipartimento di Astronomia, Università di Bologna, via Ranzani 1, I-40127 Bologna, Italy

ABSTRACT

Hydrodynamic simulations predict that a significant fraction of the gas in the current Universe is in the form of high temperature, highly ionized plasma emitting and absorbing primarily in the soft X-ray and UV bands, dubbed the Warm-Hot Intergalactic Medium (WHIM). Its signature should be observable in red-shifted emission and absorption lines from highly ionized elements. To determine the expected WHIM emission in the soft X-ray band we used the output of a large scale hydrodynamic SPH simulation to generate images and spectra with angular resolution of 14" and energy resolution of 1 eV.

The current biggest limit of any hydrodynamic simulation in predicting the X-ray emission comes from metal diffusion. In our investigation, by using four different models for the WHIM metallicity we have found a strong dependence of the emission on the model used, with differences up to almost an order of magnitude. For each model we have investigated the redshift distribution and angular scale of the emission, confirming that most photons come from redshift $z < 1.2$ and that the emission has a typical angular scale of less than a few arcminutes.

We also compared our simulations with the few currently available observations and found that, within the variation of the metallicity models, our predictions are in good agreement with current constraints on the WHIM emission, and at this time the weak experimental constraints on the WHIM emission are not sufficient to exclude any of the models used.

Subject headings: methods: numerical, intergalactic medium, diffuse radiation, large-scale structure of universe, X-rays: diffuse background, radiation mechanisms: thermal

¹corresponding author, galeazzi@physics.miami.edu

1. Introduction

The problem of the missing baryonic matter in the nearby Universe is still open. On one side we have the observations of the Lyman alpha forest at red-shift $z = 2$, the results from the WMAP experiment, and the prediction of the standard nucleosynthesis model. They all suggest a baryonic density Ω_B , expressed as fraction of the critical density, being about 0.045 Rauch et al. (1998); Weinberg et al. (1997); Burles & Tytler (1998); Kirkman et al. (2003); Bennett et al. (2003); Spergel et al. (2007); Komatsu et al. (2009). On the other side, from the observed mass distribution function of stars, galaxies and clusters, the measured baryonic fraction of the local universe comes out about 2 to 4 times lower Fukugita et al. (1998). In recent years large-scale cosmological hydrodynamic simulations Cen & Ostriker (1999a); Croft et al. (2001); Davé et al. (2001); Yoshikawa et al. (2003); Borgani et al. (2004); Cen & Ostriker (2006) allow us to trace the history of baryons from very high redshifts to $z = 0$, and they all predict that almost 50 % of the baryonic mass in the nearby Universe is in the form of a filamentary structure of gas at a temperature in the range of 10^5 - 10^7 K, the Warm-Hot Intergalactic Medium (WHIM). This gas is highly ionized and can be observed in the soft X-ray band (0.1 – 1 keV) and in the Far UltraViolet (FUV) band. Soft X-rays probe mostly gas at $T > 10^6$ K, while FUV are a better probe for gas at $T < 10^6$ K. If we assume thermal and ionization equilibrium, thermal emission models that comprise bremsstrahlung and emission lines Raymond & Smith (1977), in the approximation of thin gas, predict that most of the emission from the WHIM (considering an average metallicity of the order of $0.1 Z_\odot$) should be in the form of emission lines of highly ionized metals (O, N, C, ...).

Surveys of the sky in the soft X-ray band Snowden et al. (1997); Mushotzky et al. (2000); McCammon et al. (2002); Galeazzi et al. (2007); Henley & Shelton (2008) identify different contributions to the Diffuse X-ray Background (DXB), with local components like Solar Wind Charge Exchange, Local Bubble, and Galactic Halo, and extragalactic components, mainly AGN. A detailed inventory of the contribution from the different sources shows that there is still a fraction between 10% and 20% that could be due to a different source, such as the WHIM.

Observations in both X-rays and FUV found evidence of O VI, O VII, and O VIII absorbers from the Local Group WHIM Fang et al. (2003); Nicastro et al. (2002, 2003); Rasmussen (2002); Sembach et al. (2003); Williams et al. (2005, 2006, 2007); Bregman et al. (2009). Observations with the *Far Ultraviolet Spectroscopic Explorer* and the *Hubble Space Telescope* found almost a hundred O VI absorbers at redshift $z < 0.5$ along the lines of sight of ~ 30 AGN Danforth & Shull (2005, 2008); Tripp et al. (2008), with a $dN_{\text{OVI}}/dZ \sim 15$, together with N V, C III, C IV, Si III, Si IV, and Fe III. These absorbers can be associated to

shock-heated gas at $T \sim 10^{5.5}$ K, although there are claims that part of them could be associated to photoionized gas at $T < 10^{4.5}$ K Tripp et al. (2008). Using O VI as best tracer for this gas and assuming collisional equilibrium (CIE), ionization fraction $f(\text{O VI}) = 0.22$, and metallicity $0.1Z_{\odot}$ one obtains a detected $\Omega_{\text{OVI-WHIM}}/\Omega_B \sim 0.1$ but, depending on the assumptions on metallicity, this fraction could be higher Danforth & Shull (2008). This leaves up to $\sim 50\%$ of low redshift baryons that still need to be accounted for Danforth & Shull (2008). They are predicted to be in the form of the warmer WHIM ($10^6 < T < 10^7$ K), visible in the soft X-rays and having as primary tracers O VII and O VIII.

X-ray observations are more difficult than in FUV because of instrumental limits. So far there are claims for only four detections in absorption. Two O VII absorbers along the line of sight of Mrk 421 were identified with *Chandra* Nicastro et al. (2005), but not confirmed by *XMM-Newton* Rasmussen et al. (2007). An O VIII absorber has been detected at $z \sim 0.55$ towards PKS 2155-304 Fang et al. (2002, 2007), while another O VII absorber has been identified in the Sculptor Wall at a redshift range of $0.028 - 0.032$ Buote et al. (2009).

Detecting the WHIM in emission is even harder, since its contribution is at most 20% of the total DXB and present time instruments are not suited to identify its weak signal. However it is possible to analyze global statistical properties of the WHIM, or to identify filaments of WHIM where they are expected to be very strong. Recent observations found the WHIM signature in the X-ray angular correlation function obtained from *XMM-Newton* images Galeazzi et al. (2009). Furthermore, an *XMM-Newton* pointing in the region between clusters Abell 222 and Abell 223 found evidence of excess emission attributed to a filament connecting them Werner et al. (2008).

In this paper we use the cosmological hydrodynamic simulation by Borgani et al. (2004) to predict the X-ray emission from the WHIM. Compared to our previous work Ursino & Galeazzi (2006), we exploited the good spatial resolution (on the order of the adopted gravitational softening of $7.5 \text{ h}^{-1} \text{ kpc}$, compared to the $\sim 195 \text{ h}^{-1} \text{ kpc}$ resolution element used by Cen & Ostriker 1999) of a Lagrangian simulation to create high resolution maps of the baryon distribution.

We focused our attention on the effect of the metallicity model used on the X-ray emission. Metallicity in the filaments is one of the greatest uncertainties in this type of simulations. Observations of the intergalactic medium put some limits on metals in the InterGalactic Medium (IGM). At $z \lesssim 0.5$ groups and clusters have metallicity $Z \sim 0.3 Z_{\odot}$, while Ly- α clouds have $Z \sim 0.1 Z_{\odot}$ with a large scatter ($0.01 < Z/Z_{\odot} < 1$). Going at higher redshifts metallicity becomes lower, possibly by a factor 10 already at $z \approx 3$ Finoguenov et al. (2003); Prochaska et al. (2004); Simcoe et al. (2006). From the analysis of the low redshift O VI absorbers, colder WHIM structures have $Z \sim 0.15 Z_{\odot}$ Danforth & Shull (2008).

Although there is a possible correlation between higher metallicities and higher densities, a simple modeling of IGM metallicity is difficult. At present time it is even uncertain if there was an early metal enrichment ($z \approx 4$), if metals in the IGM are due to the newborn ($z < 2$) galaxies, or if metal enrichment history is described by a mixture of the two models Aguirre & Schaye (2005). Cosmological simulations with an accurate physical description (galactic winds, star formation, black hole feedback, and so forth) can come to an avail in reproducing the proper metallicity Cen & Ostriker (1999b); Borgani et al. (2004); Cen & Ostriker (2006); Tornatore et al. (2009); Wiersma et al. (2009b). These models predict that the average WHIM metallicity is of the order of $0.1 Z_{\odot}$ but the behavior as a function of density changes widely from simulation to simulation. Due to the lack of tight constraints on metallicity from both observations and simulations, we allowed our code to work with a set of metallicity models, in addition to the one coming directly from the Borgani simulation. Thanks to this degree of freedom we were able to investigate the dependence of the soft X-ray emission on the different metallicity models.

The paper is structured as follows. In § 2 we introduce the hydrodynamic cosmological simulation, in § 3 we describe the code we used to simulate the X-ray emission in a selected field of view, in § 4 we show the simulated images and spectra, in § 5 we discuss how the emitted spectra depend on the metallicity models.

2. The hydrodynamic Model

The general properties of the cosmological model are described in details in Borgani et al. (2004) and references therein. The simulation uses a flat Λ cold dark matter (Λ CDM) model with cosmological constant $\Omega_{\Lambda} = 0.7$, $\Omega_{\text{m}} = 0.3$, and a baryon density $\Omega_{\text{b}} = 0.04$, the Hubble constant is $H_0 = 100 \text{ h km s}^{-1} \text{ Mpc}^{-1}$, with $h = 0.7$, and $\sigma_8 = 0.8$. The Plummer-equivalent gravitational softening was set as $\epsilon_{\text{Pl}} = 7.5 \text{ h}^{-1} \text{ kpc}$. The code used to perform the simulation is the TREESPH code GADGET-2 Springel et al. (2001); Springel (2005). The simulation follows the evolution of 480^3 dark matter (DM) particles and as many baryonic gas particles from redshift $z = 49$ to $z = 0$. The box for the simulation is a cube of side $192 \text{ h}^{-1} \text{ Mpc}$, the DM and gas particles have initial masses $m_{\text{DM}} = 4.62 \times 10^9 \text{ h}^{-1} \text{ M}_{\odot}$ and $m_{\text{gas}} = 6.93 \times 10^8 \text{ h}^{-1} \text{ M}_{\odot}$ respectively. The physical processes involved in the simulation are gravity, non-radiative hydrodynamics, star formation, feedback from SNe with the effect of weak galactic outflows, radiative gas cooling and heating by a uniform, time-dependent, photoionizing ultraviolet background.

The treatment of radiative cooling assumes an optically thin gas in CIE and uses only the primordial abundances (hydrogen mass fraction $X = 0.76$, helium $Y = 0.24$). Metals

generated by the simulation itself are not considered for radiative cooling. A uniform, time-dependent UV background Haardt & Madau (1996) reionizes the Universe at $z \sim 6$.

Star formation is introduced following a hybrid multiphase model for the interstellar medium Springel & Hernquist (2003). The interstellar medium, where star formation takes place, is represented as cold clouds (cold gas) embedded in a hot gas. Clouds are not accounted for individually in a given star-forming particle, but rather they are treated all together as a fraction of the total mass of the given star-forming particle. Every gas particle is considered as composed of two parts, the hot gas, with its own mass and density, and the cold cloud fraction, temperature and density determine the relative abundances of the two components. Whenever star formation takes place, a new star particle is spawned (with just a fraction of the starting gas particle), thus increasing the number of star particles. Stars are created, following a Salpeter initial mass function Salpeter (1955), and instantly produce metals and release energy as supernovae. Metals and energy are carried to the intracluster and intergalactic medium by galactic winds. Winds are introduced in the simulation as mass outflows with rate equal to twice the star formation rate and with a wind velocity of 360 km s^{-1} .

The output of the simulation consists of 102 boxes, equally spaced in the logarithm of the expansion factor between $z = 9$ and $z = 0$. As shown in previous work (e.g., Ursino & Galeazzi (2006)) the X-ray emission above redshift 2 is negligible. For our work we therefore only used the simulation up to redshift 2.

Besides the improvement in spatial resolution compared to our previous work, this simulation suites well our needs due to its large scale that allows us enough statistics for distant regions. More recent cosmological simulations have box sizes of at most $100 \text{ h}^{-1} \text{ Mpc}$ Cen & Ostriker (2006); Oppenheimer & Davè (2008); Tornatore et al. (2009); Wiersma et al. (2009b), reducing the simulated sky area by at least a factor 3.

From the analysis of the baryonic matter we decided to group the gas particles in five phases, depending on density and temperature. At temperatures below 10^5 K we defined two phases, a dense (overdensity $\rho/\langle\rho\rangle > 1000$) cold phase associated to matter undergoing star formation, and a cold low density ($\rho/\langle\rho\rangle < 1000$) gas that corresponds to the diffuse gas that resides in the voids of the web structure of the Universe, and that has been identified with the Ly α absorbers. For intermediate temperatures ($10^5 < T < 10^7 \text{ K}$) we have the warm hot gas. Also in this case we defined two phases, the low density one ($\rho/\langle\rho\rangle < 1000$) that roughly corresponds to the filamentary structure of the WHIM, and the high density ($\rho/\langle\rho\rangle > 1000$) gas, associated with groups of galaxies. Finally, at $T > 10^7 \text{ K}$, we identify clusters of galaxies and the hot intracluster medium (ICM). Fig. 6 shows the phase diagram in the temperature-density space. The choice of the threshold between diffuse and dense

WHIM is somewhat arbitrary and different authors have used different thresholds in the range $100 < \rho/\langle\rho\rangle < 1000$. For consistency with a significant fraction of the literature, including our previous work (Ursino & Galeazzi 2006), we adopted the definition of Cen & Ostriker (1999b).

3. The Simulation

To create a simulated light cone up to redshift 2, we adopted a procedure similar to the one described in Roncarelli et al. (2006), where several boxes from the output snapshots of the Borgani simulation were piled one after the other. Since the boxes have side of $192 \text{ h}^{-1} \text{ Mpc}$, the redshift interval covered by each box is $\Delta z_s \gtrsim 0.06$ (increasing at higher redshift). The time-step between two consecutive snapshots of the Borgani simulation corresponds to $\Delta z_t \gtrsim 0.02$ at small redshift, increasing at higher redshift, therefore Δz_s corresponds to the time-step between three consecutive snapshots. For our simulation we created one box taking slices of $64 \text{ h}^{-1} \text{ Mpc}$ from three consecutive snapshots as shown in Fig. 6. This allows to better follow the evolution of the gas. Since consecutive boxes represent the same structure evolved in time and they do not change much for small redshift intervals, particular attention was given to avoiding encountering the same structures at different redshifts. We therefore used random rotations around the line of sight axis, random permutations of the coordinate axes of each composite box, and random shifts along the three axes. These randomizations give a very large number of degrees of freedom to avoid periodicity. The downside of this procedure is that it introduces discontinuities between two adjacent snapshots. Although these discontinuities are unphysical, their effect on our simulation is minor due to the very small probability of finding a significant WHIM structure right at the edge of the SPH box.

The last step in the simulation is piling up the modified cubes to form a simulated light cone. Fig. 6 shows a representation of a simulated light cone, with superposed a selected field of view. The code itself is capable of spanning any distance as long as the angle of the field of view is smaller than the angular size of the last box, but we chose a maximum corresponding to redshift $z = 2$, equivalent to 19 cubes. Emission from greater distances is expected to be a small fraction of the total emission, while at the same time the calculation drastically increases the computing time. The angular size of the furthest box, which determines to largest field of view that can be constructed in a single simulation, is $\sim 2.1^\circ \times 2.1^\circ$. The typical field of view used is $1^\circ \times 1^\circ$.

The field of view starts from the center at the bottom of the first box, and only particles that are inside such field of view (see Fig. 6) are selected. Besides this geometrical filter, we

adopted two more filters. Since baryons at $T < 10^5$ K do not emit any significant amount of X-rays, we filtered out all the particles with temperature lower than this limit to speed up the computational process. At $z = 0$ the diffuse warm gas and the star forming gas cover $\sim 50\%$ of the gas mass (roughly $\sim 50\%$ of the particles) and that this fraction increases to $\sim 75\%$ at $z = 2$. Our filter therefore reduces the computational time by more than a factor of 2. One more final filter discriminates between particles of the three remaining warm-hot phases and labels them accordingly.

For temperatures in the range $10^5 < T < 10^7$ K the two main sources of radiation between 0.1 and 1 keV are thermal bremsstrahlung and emission lines from highly ionized elements (i.e. C v, C vi, O vii, O viii, Ne ix, Mg xi, and Fe xvii), although our investigation is focused on O vii and O viii. In order to properly evaluate emission from the lines, it is necessary to set metal abundances.

As we stated previously, we designed the program with the capability of working with different metallicity models, in addition from the original metallicity predicted by the hydrodynamic code. This choice is aimed at overcoming the lack of precise information about metal formation and metal diffusion in the intergalactic medium, and to compare the x-ray emission expected from different metal distributions.

The first metallicity model (from now on defined as “Borgani model”) we adopted is the original model coming from the Borgani (2004) simulation. This model underestimates the diffusion of metals in most of the WHIM, assigning metals to only a fraction of the gas particles. The reason of the uneven distribution of metals in the WHIM depends on the treatment of metal diffusion in SPH simulations, as it is well explained in Fig. 4 of Wiersma et al. (2009b). An SPH star-forming particle enriches the neighboring particles and they are driven away by the energy released by stars in the star particle. The metal enriched particles mix with metal-free gas particles, but do not enrich them since there is no diffusion from gas particles. Therefore the metal distribution is not evenly smoothed, but concentrated in the few gas particles that have been directly enriched by star-forming particles. As a result most of the WHIM is poor in metals and its emission is underestimated. This can be avoided if a model of diffusion of metals from one particle to the others is included in the simulation, which is not the case of the simulation we used.

In addition to the metallicity extracted from the Borgani model, we used three analytical models based on relations between metallicity and density (see Fig. 6).

The first analytical model (defined as “Croft model”) links the metallicity directly to the gas density, using the relation $Z \propto (\rho/\bar{\rho})^{1/2}$. Metallicity is normalized to $Z = 0.005 Z_{\odot}$ at $\rho = \bar{\rho}$, so that it matches the measured metallicity of the Ly- α forest, while an upper limit

of $Z = 0.3 Z_{\odot}$ fits well with data on clusters Fang et al. (2005). This model is in agreement with the metallicity predicted by Cen & Ostriker (1999a) at $z = 3$ and is about a factor 5 lower than the IGM metallicity at more recent times. Nevertheless we adopted this model as comparison since it has also been used by other authors Croft et al. (2001); Fang et al. (2005).

The second analytical metallicity model (which we called the “Scatter model”) is based on the distribution function of metallicity from Cen and Ostriker (1999b) at redshift $z = 0$. Part of the output of that simulation consists of three boxes of 512^3 cells with values of temperature, density, and metallicity. Using the three boxes we generated the probability distribution function of metallicity as a function of density, where metallicity is divided in 110 intervals from 10^{-7} to $10^4 Z_{\odot}$ and density is divided in 70 intervals from 10^{-3} to $10^4 \rho_b$. When this model is selected, the code reads the density of each particle and assigns a random metallicity based on the probability distribution function at the corresponding density. The average distribution of metallicity for this model is represented by the black curve in Fig. 6. This model has the highest metallicity among the four models (a factor 2–3 for overdensities between 10 and 1000) and, since at first order the intensity of the lines depends linearly on metallicity, we use the emission with the scatter model as an upper limit for our set of simulations.

The third analytical metallicity model, labeled “Cen model”, is an improved version of the scatter model, where we also include redshift dependence evaluated from Fig. 2 of Cen & Ostriker (1999b). A “random” metallicity is initially evaluated following the same procedure used for the scatter model, then it is modified according to redshift of the particle. We note that the redshift dependence of the metallicity is optimized for WHIM particles and would overestimate the metallicity of clusters and groups. By definition the average values of the Cen model at $z=0$ are identical to those of the scatter model. To show the redshift variation, in Fig. 6 we plot the average values of the Cen model at $z = 0.5$, and $z = 1$ in tones of gray. We introduced this model for two main reasons: to evaluate the influence of time evolution on metallicity and to compare the predictions of this model with the results of our previous work Ursino & Galeazzi (2006), where we used the same fitting function to estimate time evolution of metallicity.

We stress the fact that in the original Borgani simulation the cooling function does not depend on metals but only on primordial abundances and that the models of metallicity that we adopt, are introduced *a posteriori* and do not affect the baryon history. It has been shown that including a self consistent metal dependence in a simulation increases the cooling rates, resulting in a lower emission (above all for strongly emitting gas) than what is predicted using only primordial abundances, even by an order of magnitude Bertone et al. (2010).

The following step is to calculate the spectrum of emitted photons, as a function of electron number density n_e , temperature T and metallicity Z for every SPH particle. We did not consider peculiar velocities. Velocities of a few hundred km s^{-1} correspond to $\Delta z \sim 0.001$, more than a factor 30 less compared to the redshift interval between two boxes. These velocities correspond to displacements of the emitters of less than 10 Mpc, if we attempt to estimate the distance from the redshifted spectrum of an absorber. We used the XSPEC version of the APEC model¹ Smith et al. (2001) using solar relative abundances to produce the spectra, in the assumption of an optically thin gas in CIE and no photo-ionization from a background radiation. We assumed CIE since we expect to probe the WHIM mainly in regions at higher temperature and density, where the ionization balance is dominated by collisions. Models show that the WHIM could depart from ionization equilibrium Yoshida et al. (2005); Cen & Fang (2006) and the abundances of ions in the case of non-equilibrium are generally higher Gnat & Sternberg (2007), however the expected differences between the observables in ionization equilibrium and non-equilibrium are small Yoshikawa & Sasaki (2006). In details, our procedure goes as follows. We created a grid of spectra as a function of temperature and metallicity, equally spaced on a logarithmic scale both in temperature between 10^5 K and 10^8 K, and metallicity Z between $5 \times 10^{-4} Z_\odot$ and $5 Z_\odot$ respectively. We set the energy resolution at 1 eV between 0.05 and 3 keV, and at 50 eV between 3 and 50 keV. We interpolated from the grid, using the temperature and metallicity of a given SPH particle to compute a reference spectrum $\Lambda_{T,Z}(E_0)$, with E_0 the rest-frame energy. Then we calculated the emitted spectrum, corresponding to the number of emitted photons per unit of time, with the formula

$$s_0(E_0) = x_e n_H^2 V \Lambda_{T,Z}(E_0) , \quad (1)$$

where V is the physical volume of the particle (defined as mass of the particle divided by density), n_H is the number density of hydrogen nuclei (given by the SPH simulation), and the density of electrons is given by $n_e = x_e \times n_H$, with $x_e = 1.225$ (assuming near full ionization).

Finally we computed the observer-frame spectrum $s(E)$, applying the energy redshift $E = E_0(1 + z)$ to $s_0(E_0)$, and the corresponding flux in each energy channel

$$S(E) = \frac{s(E)}{4\pi d_c^2(1 + z)} , \quad (2)$$

where d_c is the comoving distance of the particle from the observer and the factor $(1 + z)$ accounts for the redshift dimming of the signal.

This quantity is then distributed in the different map pixels by using the SPH smoothing

¹<http://heasarc.gsfc.nasa.gov/docs/xanadu/xspec/>

kernel

$$w(r) \propto \begin{cases} 1 - 6r^2 + 6r^3, & 0 \leq r \leq 0.5 \\ 2(1 - r)^3, & 0.5 \leq r \leq 1 \\ 0, & r \geq 1, \end{cases} \quad (3)$$

where $r \equiv \Delta\theta/\alpha_h$ is the angular distance from the particle position in the map, in units of the angle α_h subtended by the particle smoothing length provided by the hydrodynamic code. In this kind of computation the smoothing procedure results to be the most time consuming. However the mathematical properties of the smoothing function can help speeding up the computation. First of all, since the function of eq. 3 is the approximation of a 2-dimensional Gaussian in the sky plane, the distribution can be separated into the product of its two components along the map axis, $w(r) \simeq w(x) \times w(y)$. Then, since the function is integrable, we can directly define $W(x) \equiv \int_{-1}^x w(\tilde{x})d\tilde{x}$ and use it for the computation. The normalization of $w(x)$ is chosen to have $W(1) = 1$. Therefore, for a given pixel (i, j) we compute its corresponding flux fraction

$$f_{i,j} = [W(x_1) - W(x_0)] \times [W(y_1) - W(y_0)] , \quad (4)$$

where (x_0, y_0, x_1, y_1) identify the pixel limits in the two directions. We highlight also the fact that our definition of $W(x)$ ensures that $\sum_{i,j} f_{i,j} = 1$ without the need to renormalize it.

This procedure is done separately for the three gas phases (WHIM, dense WHIM, and hot gas) in order to keep the information about their different contributions.

The final result of the simulations is a three dimensional array (the two angular coordinates and the energy) for each gas phase (Hot, WHIM, and Dense WHIM) containing photon counts per second per cm^2 . We also saved one array for each box used to build the simulated light cone, so that we have information about the spectrum as a function of redshift.

At the end of the process we included the absorption due to the neutral hydrogen in our galaxy using the model described by Morrison and McCammon (1983), with a typical value at high latitude of $n\text{H} = 1.8 \times 10^{20} \text{ cm}^{-2}$ McCammon et al. (2002).

4. Results

The imaging capability of the simulation gives us the opportunity to study the WHIM morphology and emission, or focus on the properties of individual objects. We can also extract energy spectra for every pixel of the image.

As an example of the capabilities of our simulations, Figs. 6 and 6 show images in the energy band 380 – 950 eV, with a field of view of $1^\circ \times 1^\circ$ and 256×256 pixels, with an

angular resolution of $14'' \times 14''$. The simulation runs to a distance equivalent to $z = 2$.

The energy band $380 - 950$ eV is adopted throughout all the paper, unless otherwise stated, and is the same as the one we used in our previous work Ursino & Galeazzi (2006). We chose the upper limit to include the emission from Ne IX at 921 eV and the strong Fe XVII lines in the energy band $0.725 - 0.827$ keV, while with the lower we could exclude the strong C V and C VI lines at 0.308 keV and 0.367 keV respectively. This makes us sensitive to O VII out to redshifts of $z=0.5$. It is also advantageous to avoid instrumental effects due to the neutral carbon absorption edge at 0.284 keV, which is present in most instruments.

The angular resolution is a trade-off between the requirements of accuracy and computing resources. In our previous work we have shown that the detected WHIM emission depends on the angular resolution Ursino & Galeazzi (2006). We have seen that the characteristic angular size of filaments is of the order of a few arcminutes and that with a coarse resolution the probability of detecting individual WHIM filaments becomes negligible. Similarly, a more detailed analysis on the effect of the angular resolution has also been reported in Bertone et al. (2010). The chosen angular resolution is well below the typical WHIM scale as indicated in both papers, and should allow a good, unbiased characterization of the angular distribution of the WHIM emission.

For this exercise we generated images for each of the three gas phases, for each redshift slice corresponding to a box of the hydrodynamic simulation, and for the full line of sight, and we selected a region in the image to extract the relative spectra for different circular FoVs. Looking at the images of the slice in the redshift interval $0.201 - 0.273$ (Fig. 6), the different nature of the three phases is clear. The WHIM is collected in large, diffuse regions and is sparse throughout the whole image in filaments. The dense WHIM is grouped in much more compact objects, and is found in the inner part of the WHIM regions, where it traces the WHIM filaments. The hot gas is found in few large objects, close to the regions where the WHIM emission is stronger. The general picture confirms the assumption that was made when we defined the three phases. The hot gas is associated to the big clusters of galaxies while the dense WHIM corresponds to the groups of galaxies. The diffuse WHIM, on the other side, appears mostly as haloes that envelope the groups. As it should be expected, when the contribution at all redshifts is included, the filamentary structure of the WHIM is partially hidden in these images (Fig. 6). This is due to the large energy interval used in the generation of these images. However, when the energy information is taken into account by focusing for example on a narrow energy interval containing the redshifted O VII line, the spatial information about the three phases can still be extracted. Figure 6 shows the image obtained by generating an image of the full line of sight for the narrow energy band corresponding to the energy of O VII lines with redshift between 0.201 and 0.273. Notice that

we obtain the same spatial information of Fig. 6 for the WHIM, while the hot and dense sources are more compact than for the full energy band. In the case of dense sources this indicates that we see O VII emission mostly from their core. With the hot sources, on the other side, although we are indeed probing the O VII band, we actually see photons emitted via bremsstrahlung, which dominates (in this band) at high temperatures.

Figure 6 shows the spectra extracted from the selected fields of view in figures 6 and 6, along the full line of sight. We can use it to set a limit on the angular resolution required to study the WHIM. The 1' field of view is centered on a WHIM filament. The spectrum shows O VIII emission lines from the selected filament, together with lines emitted by baryons at different redshifts. When we increase the field of view to 3', we also find the O VII line from a different region of the filament. At the same time the overall flux from the WHIM at all redshifts increases due to the contribution of other regions, making it more difficult to identify the signal of the filament being studied. At even larger fields of view, the lines from the filament are overshadowed by the total WHIM flux. This indicates that, at redshift $z \sim 0.25$, an angular resolution of a few arcminutes is necessary in order to detect a filament. A more systematic investigation of the angular distribution of the WHIM emission is discussed in the next section.

The spectrum on the right side of Figure 6 shows that the emission of the dense WHIM and the hot gas is stronger than the WHIM, and the flux is between 5 and 10 times higher. It is important to note that the cluster contribution to the spectrum in the soft X-rays is mostly due to bremsstrahlung. To separate the WHIM from these two phases we need to identify the emission lines, and this sets the requirement on the energy resolution of any instrument designed to study the WHIM. An energy resolution of a few eVs is necessary to resolve single lines, in particular if we want to identify the O VII triplet at ~ 570 eV, the main tracer of the WHIM.

5. X-ray Emission and Metallicity

We generated four sets of identical simulations, with the metallicity as the only parameter that was changed, using the models described in section 3. For simplicity we refer to those models as “Borgani”, “Croft”, “Scatter”, and “Cen”.

To evaluate the contribution of the WHIM to the total diffuse X-ray emission we compared our simulations with results from the X-ray Quantum Calorimeter (XQC) sounding rocket program (McCammon et al. 2002) and the *ROSAT* All Sky Survey (RASS - Snowden et al. 1994). XQC is the only current mission using high resolution microcalorimeters

for the study of the DXB in the energy range 50-2000 eV, while RASS is the most accurate X-ray survey below 1 keV and are considered the benchmarks for any soft DXB studies. The most recent XQC published results (McCammon et al. 2002) predict a surface brightness of $29.3 \text{ photons cm}^{-2} \text{ s}^{-1} \text{ sr}^{-1}$ in the 0.380-0.950 keV energy band. In table 1 we report the surface brightness predicted by the four simulations in the same energy band and the predicted flux in the RASS *R4* and *R5* bands (Snowden et al. 1994) in units of $10^{-6} \text{ photons s}^{-1} \text{ arcmin}^{-2}$ (the default RASS units). The average RASS flux in the *R4+R5* bands is $\sim 139 \cdot 10^{-6} \text{ photons s}^{-1} \text{ arcmin}^{-2}$. The Borgani model has the lowest brightness, $0.77 \pm 0.04 \text{ photons cm}^{-2} \text{ s}^{-1} \text{ sr}^{-1}$ in the 0.380-0.950 keV energy range, and can be used to put a lower limit to the WHIM emission. We remind that even if this model has a high average metallicity at low densities (as shown in Fig. 6 and table 1), most of the particles actually have no metals due to the poor diffusion of metals to low density regions in the hydrodynamic code. Moreover, the few particles with metals have low density and, since emission goes as density squared, they give little contribution as well.

The Croft model predicts a relatively low emission as well, $1.84 \pm 0.08 \text{ photons cm}^{-2} \text{ s}^{-1} \text{ sr}^{-1}$. This model was designed to work at high redshift ($z \sim 3$), where the gas is still rather poor in metals. Although being somewhat unrealistic, this model is a test of intermediate metallicity.

The Scatter model, on the other hand, was created for gas at $z = 0$, and slightly overestimates the observed metallicities at $0 < z < 0.5$ ($Z \sim 0.3Z_{\odot}$ for groups and clusters and $Z \sim 0.1Z_{\odot}$ for diffuse gas, as seen in § 1), but it gives much higher metallicities (possibly up to a factor 10) than what is measured at higher redshift ($0.5 < z < 2$). The average surface brightness is $4.3 \pm 0.2 \text{ photons cm}^{-2} \text{ s}^{-1} \text{ sr}^{-1}$. This value is the highest predicted by the set of simulations and we use this as an upper limit to the flux.

Using the Cen metallicity model, the simulation predicts a surface brightness of $4.2 \pm 0.2 \text{ photons cm}^{-2} \text{ s}^{-1} \text{ sr}^{-1}$. All the values are smaller than what we obtained in our previous work Ursino & Galeazzi (2006) where, using the hydrodynamic model by Cen and Ostriker, (1999a) we obtained a predicted brightness of $6.9 \pm 0.9 \text{ photons cm}^{-2} \text{ s}^{-1} \text{ sr}^{-1}$. It must be noted that in the previous work we analytically extrapolated the values of temperature, density, and metallicity from the dataset at $z = 0$ as it was the only dataset available. It is therefore possible that the evolution of the gas is rather different than what is used in the current simulations.

Focusing on the O VIII line at 650 eV in Fig. 15 of McCammon et al. (2002) we see that, if we consider the local foreground and the AGNs component, there is still room for an extragalactic contribution of $\sim 9 \text{ photons cm}^{-2} \text{ s}^{-1} \text{ sr}^{-1} \text{ keV}^{-1}$ ($\sim 0.09 \text{ photons cm}^{-2} \text{ s}^{-1} \text{ sr}^{-1}$ if we assume an energy interval $\Delta E = 10 \text{ eV}$). In the same band, our four metallicity models predict a surface brightness of $9.9E - 3 \pm 0.6E - 3 \text{ photons cm}^{-2} \text{ s}^{-1} \text{ sr}^{-1}$, $0.025 \pm$

0.002 photons $\text{cm}^{-2} \text{s}^{-1} \text{sr}^{-1}$, 0.059 ± 0.004 photons $\text{cm}^{-2} \text{s}^{-1} \text{sr}^{-1}$, and 0.058 ± 0.004 photons $\text{cm}^{-2} \text{s}^{-1} \text{sr}^{-1}$ respectively, all within the limits of the X-ray Quantum Calorimeter (XQC) sounding rocket data McCammon et al. (2002).

The two higher metallicity models predict values that are half of the ROSAT data in Fig. 1 of Kuntz et al. (2001). The absorbed extragalactic component in the 380 – 950 eV, in fact, has an almost constant value of $\sim 10 \text{ keV cm}^{-2} \text{s}^{-1} \text{sr}^{-1} \text{keV}^{-1}$, corresponding to ~ 8.8 photons $\text{cm}^{-2} \text{s}^{-1} \text{sr}^{-1}$.

Recently Hickox and Markevitch (2007) quantified the unresolved XRB in the Chandra deep fields as $(1.0 \pm 0.2) \times 10^{-12} \text{ ergs cm}^{-2} \text{s}^{-1} \text{deg}^{-2}$ in the 0.65 – 1 keV band. Although these measurement were performed in a very limited region of the sky (a circle of radius 3.2'), this value constitutes an upper limit to the WHIM emission. All of our models fall below this limit, predicting, in the same band $(6.5 \pm 0.4) \times 10^{-14} \text{ ergs cm}^{-2} \text{s}^{-1} \text{deg}^{-2}$, $(1.5 \pm 0.1) \times 10^{-13} \text{ ergs cm}^{-2} \text{s}^{-1} \text{deg}^{-2}$, $(3.3 \pm 0.3) \times 10^{-13} \text{ ergs cm}^{-2} \text{s}^{-1} \text{deg}^{-2}$, and $(3.2 \pm 0.3) \times 10^{-13} \text{ ergs cm}^{-2} \text{s}^{-1} \text{deg}^{-2}$ respectively.

The results obtained with the Borgani model can also be compared with Roncarelli et al. (2006), who obtained an estimates on the DXB starting from the same cosmological simulation and with a similar method. They obtain $5 \times 10^{-13} \text{ ergs cm}^{-2} \text{s}^{-1} \text{deg}^{-2}$ in the same band (as extrapolated by Hickox & Markevitch 2007), thus almost an order of magnitude higher than the $(6.5 \pm 0.4) \times 10^{-14} \text{ ergs cm}^{-2} \text{s}^{-1} \text{deg}^{-2}$ obtained with the Borgani model, although within the observational upper limit. This difference is due to the fact that Roncarelli et al. (2006) adopted an observationally oriented approach by excluding from their maps the extended sources detected by Chandra observations. This means that their estimate includes also the emission from unresolved clusters and groups (corresponding to our hot and dense WHIM phases, respectively) that are instead excluded in our estimate.

Measurements of the autocorrelation function for a set of XMM-Newton observations Galeazzi et al. (2009) point to the fact that the X-Ray emission in the 0.4 – 0.6 keV band from the WHIM is $12 \pm 5\%$ of the total extragalactic diffuse emission. Our models predict $10 \pm 1\%$, $12 \pm 1\%$, $17 \pm 1\%$, and $13 \pm 1\%$, in agreement with the observational data.

In order to understand the dependence of flux from metallicity and redshift of the sources, we calculated the average flux of each slice of the simulations and compared with the results of our previous work Ursino & Galeazzi (2006). Figure 6 clearly shows that, while the overall photon budget is comparable between the old and new analysis, the dependence on redshift behaves in very different ways, being much steeper in the case based on Cen & Ostriker (1999a) simulations. Focusing on the data from the current simulation, we see that the dependence from redshift changes with metallicity model. The four models show the

same trend, with a rather slow decrease of photon flux at increasing redshift (compared to the older simulations), but the relative steepness is different. For the Borgani metallicity, photons coming from low redshift are ten times more than those coming from very high redshift, in the case of Croft metallicity the ratio of photons from near sources over photons from distant sources is around 20, and for the highest metallicity models this ratio is of the order of ~ 30 . Since in our models metallicity depends directly on density, the metal abundance is higher in high density regions, where there is more star formation. At low redshift, when the Universe is older, there are more high density regions compared to the young Universe, and therefore there are more high metallicity regions. This makes the difference between the abundance of metals at low redshift and at high redshift bigger for those models where metallicity is stronger. This effect is due only to the relation between density and metallicity, and does not depend on any assumption on star formation history.

We also investigated how the potential capability of a WHIM dedicated future mission like EDGE Piro et al. (2009) or Xenia Hartmann et al. (2009). The *Wide Field Imager* (WFI) on EDGE (or Xenia - values in brackets) has a proposed field of view with diameter 1.5° (1.5°), an angular resolution of $15''$ ($10''$), an effective area of 580 (1000) cm^2 at 1 keV, and an energy resolution of 70 eV at 1 keV (70 eV at 0.5 keV). The *Wide Field Spectrometer* (WFS) on EDGE (Xenia) has a proposed field of view of $0.7^\circ \times 0.7^\circ$ ($1^\circ \times 1^\circ$), an angular resolution of $3.7'$ ($2.5'$), an effective area of 1163 (1300) cm^2 at 600 eV, and an energy resolution of 3 (1) eV at 0.5 keV. We simulated an experiment similar to the WFS, with roughly same effective area (1000 cm^2) and angular resolution ($3' \times 3'$ pixels), values close to the EDGE/Xenia goal and consistent with our previous work. Figure 6 shows the frequency of flux depending on the metallicity model. The frequency using the Borgani model is peaked at a much smaller value than the other models, and seldom finds pixels with more than 6 photons $\text{cm}^{-2} \text{s}^{-1} \text{sr}^{-1}$. The Scatter and Cen models behave almost identically. They have a broad distribution, centered at around 5 photons $\text{cm}^{-2} \text{s}^{-1} \text{sr}^{-1}$, and a long tail going over the 20 photons $\text{cm}^{-2} \text{s}^{-1} \text{sr}^{-1}$. The Croft model is somehow in between, with a peak at approximately 2 photons $\text{cm}^{-2} \text{s}^{-1} \text{sr}^{-1}$ and a tail going up to 15 photons $\text{cm}^{-2} \text{s}^{-1} \text{sr}^{-1}$. The capability of the mission to detect and study the WHIM will strongly depend on the correct metal abundance. In the case of our simulated experiment, with an exposure time of 1 Msec, assuming a total galactic foreground plus extragalactic background of ~ 29.3 photons $\text{cm}^{-2} \text{s}^{-1} \text{sr}^{-1}$ in the $380 - 950$ eV band (obtained using the three-component model by McCammon et al. 2002) and an instrumental noise of ~ 0.5 photons $\text{cm}^{-2} \text{s}^{-1} \text{sr}^{-1}$ (in the same energy band), the threshold for WHIM detection is ~ 0.6 photons $\text{cm}^{-2} \text{s}^{-1} \text{sr}^{-1}$. The probability of finding objects above such threshold is $\sim 50\%$ for the Borgani metallicity and 99% for the Scatter metallicity. The chance of finding objects with surface brightness greater than 20% of the DXB, equivalent to ~ 6 photons $\text{cm}^{-2} \text{s}^{-1} \text{sr}^{-1}$, is 20% for the Scatter and

Cen models, and negligible for the Borgani model.

Fig. 6 shows images of the WHIM at redshift $z = 0.13 - 0.20$. The ring-like shape of the bright objects is just an artifact due to the fact that X-rays coming from particles classified as hot or dense gas, which are present inside these objects, are not included in these images. The figures represent images of the same part of the sky with X-rays simulated using respectively the Borgani (top left), Croft (top right) Scatter (bottom left), and Cen (bottom right) models. Notice that the amplitude of surface brightness of the four maps changes by almost an order of magnitude going from the Borgani to the Cen metallicity model. The Croft metallicity is proportional to density, therefore brightness is a direct function of density squared. For the Scatter and Cen Models, the ratio between the mean value of metallicity at low and high density is smaller, and therefore the fainter objects are more visible. There is also the scatter effect that comes into play changing the brightness between regions with the same density. The Borgani model is strongly affected by the poor metal diffusion that leaves many particles depleted in metals, therefore there is limited contribution from lines, and the emission is characterized almost only by the continuum due to bremsstrahlung.

In Fig. 6 we show the energy spectra in the $480 - 520$ eV band extracted from two different regions of Fig. 6 where the WHIM is particularly bright. The lines correspond to the O VII triplet coming from two emitters at redshift $z \sim 0.15$. Looking at the spectra we see how the metallicity model influences the intensity of the lines. The Scatter and Cen models have the highest metallicity and they predict the strongest emission line for an O VII emitter. The lines simulated with the two models have almost the same intensity, with a little difference due to the correction to metallicity that the Cen model applies to the Scatter one. Since in this case the redshift is small and the overdensity is relatively high, the correction to metallicity is small. From Fig. 6 we see that for the Croft model the metallicity is 3–5 times lower than for the Scatter model, and the difference with the Cen model at higher redshift is smaller. The same ratio holds between the intensity of the lines in the spectra extracted and emission follows the lead of metallicity quite well. For the Borgani model things are different, as expected. The emitter in the left panel shows no sign of emission lines, even if simulations with the other models show an emitter at that position. Again, this is due to the poor metallicity distribution, this is a region where the particles of the simulation had no contact with metal rich particles and therefore have no metals at all, the emission is only in the continuum. The spectrum in the right panel shows the presence of O VII lines also for the Borgani model, showing that this region has gone through metal enrichment, even if not as much as in the case of other metallicity models.

Using maps along the full line of sight we can try to characterize the angular autocorrelation function Kuntz et al. (2001) of the three phases, in order to extract the signal of the

WHIM. So far experimental work has been done on the diffuse X-ray background Kuntz et al. (2001); Soltan et al. (2001); Giacconi et al. (2001), giving evidence of a signal at the order of less than 10 arcmin. In our previous work Ursino & Galeazzi (2006) we used WHIM maps with rather broad angular resolution (1 arcmin) and found a characteristic angle comparable with the experimental values. With the current angular resolution of $14''$ we study the angular autocorrelation function (AcF) of the WHIM at even smaller scales, and how it evolves with metallicity. Fig. 6 shows the average AcFs for the Borgani, Croft, Scatter, and Cen metallicity models, with error bars representing the cosmic variance for each set of simulated maps. They are in good agreement with each other, giving a characteristic angle of ~ 10 arcmin and well within the error bars (at this angle) of our previous work. The lower metallicity models hint to a somewhat slightly larger structure scale. The bad match with the older model has more than one reason aside from the very fact that we are dealing with different models. The older maps were smaller ($30' \times 30'$ instead of $60' \times 60'$) and the angular resolution was smaller ($1' \times 1'$, limited by the resolution of the hydrodynamic simulation). The small area gives rise to the much bigger variance and possibly to the fluctuation below 0 at $\theta > 5$ arcmin. The worse angular resolution also explains (at least in part) the steeper slope at small angular scales.

6. Conclusions

In our work we used the cosmological simulation by Borgani et al. (2004) to predict spectral and spatial properties of the WHIM. Since metallicity is the main source of uncertainties for this prediction, we used four metallicity models, one self consistent with the Borgani simulation, and three analytical models, two of them based on statistics adopted from Cen & Ostriker (1999a). The first model gives a lower limit to metallicity predictions, while the last two give a higher limit. For each model we generated a set of $1^\circ \times 1^\circ$ maps up to redshift $z = 2$.

The tools we developed allowed us to characterize the WHIM emission, obtaining the following main results:

- (i) The predicted X-ray emission from the WHIM depends strongly on the metallicity model: the strongest emission comes from the more metallic model, and it can be up to an order of magnitude stronger than from the low metallicity models. The predicted emission, in particular from high metallicity models, is in good agreement with observational data. It accounts for a fraction between 2.5% and 15% of the total DXB, and between 11% and 66% of the extragalactic emission at the energy of O VIII as measured from the XQC experiment McCammon et al. (2002). It accounts for 8%

to 49% of the extragalactic component observed with ROSAT Kuntz et al. (2001) and for 6.5% to 33% of what measured with CHANDRA Hickox & Markevitch (2007). The WHIM emission spans from 10% to 17% of the total emission, in agreement with the 12% estimated with analysis of the AcF Galeazzi et al. (2009).

- (ii) The predicted surface brightness decreases with increasing redshift of the emitting gas and most of the photons come from redshift $z < 1.2$.
- (iii) The probability distribution function of emission along a line of sight depends on metallicity. For low metallicity the distribution is narrow and peaked around its low average value, for high metallicity the distribution is wide and there are higher chances to point at bright objects (20% possibility to find an object brighter than 6 photons $\text{cm}^{-2} \text{s}^{-1} \text{sr}^{-1}$ for the statistical models).
- (iv) A simple analysis of the maps with the AcF gives a characteristic angular size of less than a few arcmin.

In summary, the prediction from our models are consistent with the constraints from observational data for all the metallicity distributions we assumed. Future mission with high energy resolution and good angular resolution will allow us to discriminate between the signals of the WHIM and of clusters of galaxies and possibly tracing the WHIM structure. Since the expected emission depends strongly on metallicity, measuring the flux from the WHIM will make possible to estimate the metal abundance of the WHIM.

This work has been supported in part by the University of Miami Small Grant Program. The authors would like to thank Stefano Borgani for the access to his hydrodynamic simulations, and to Lauro Moscardini and Enzo Branchini for the useful discussion and suggestions.

REFERENCES

- Aguirre, A., & Schaye, J. 2005, *Int. Astron. Union Symp.*, 1, 289
- Bennett, C. L., et al. 2003, *ApJS*, 148, 1
- Bertone, S., et al. 2010, *MNRAS*, online early view, DOI 10.1111/j.1365-2966.2010.16932.x
- Borgani, S., et al. 2004, *MNRAS*, 348, 1078
- Bregman, J. N., et al. 2009, *ApJ*, 699, 1765

- Buote, D. A., et al. 2009, ApJ, 695, 1351
- Burles, S., & Tytler, D. 1998, ApJ, 499, 699
- Cen, R., & Fang, T. 2006, ApJ, 650, 573
- Cen, R., & Ostriker, J. P. 1999a, ApJ, 514, 1
- Cen, R., & Ostriker, J. P. 1999b, ApJ, 519, L109
- Cen, R., & Ostriker, J. P. 2006, ApJ, 650, 560
- Croft, R. A. C., et al. 2001, ApJ, 557, 67
- Danforth, C.W., & Shull, J.M. 2005, ApJ, 624, 555
- Danforth, C.W., & Shull, J.M. 2008, ApJ, 679, 194
- Davé, R., et al. 2001, ApJ, 552, 473
- Fang, T., et al. 2002, ApJ, 572, L127
- Fang, T., Sembach, K. R., & Canizares, C. R. 2003, ApJ, 586, L49
- Fang, T., et al. 2005, ApJ, 623, 612
- Fang, T., Canizares, C. R., & Yao, Y. 2007, ApJ, 670, 992
- Finoguenov, A., Burkert, A., Bohringer, H., 2003, ApJ, 594, 136
- Fukugita, M., Hogan, C. J., & Peebles, P. J. E. 1998, ApJ, 503, 518
- Galeazzi, M., et al. 2007, ApJ, 658, 1081
- Galeazzi, M., Gupta, A., & Ursino, E. 2009, ApJ, 695, 1127
- Giacconi, R., et al. 2001, ApJ, 551, 624
- Gnat, O. & Sternberg, A., 2007, ApJS, 168, 213
- Haardt F., Madau P., 1996, ApJ, 461, 20
- Hartmann, D., Kouveliotou, C., Piro, L., et al. 2009, The Astronomy and Astrophysics Decadal Survey, Science White Papers
- Henley, D. B., & Shelton, R. L. 2008, ApJ, 676, 335

- Hickox, R. C., & Markevitch M. 2007, ApJ, 661, L117
- Kirkman, D., et al. 2003, ApJS, 149, 1
- Komatsu, E., et al. 2009, ApJS, 180, 330
- Kuntz, K. D., et al. 2001, ApJ, 548, L119
- McCammon, D., et al. 2002, ApJ, 576, 188
- Morrison, R., McCammon, D. 1983, ApJ, 270, 119
- Mushotzky, R. F., et al. 2000, Nature, 404, 459
- Nicastro, F., et al. 2002, ApJ, 573, 157
- Nicastro, F., et al. 2003, Nature, 421, 719
- Nicastro, F., et al. 2005, Nature, 433, 495
- Oppenheimer, B. D., & Davè, R. 2008, MNRAS, 387, 577
- Piro, L., den Herder J.W., Ohashi T., et al., 2009, ExA, 23, 67
- Prochaska, J. X., et al. 2004, ApJ, 617, 718
- Rasmussen, A., 2002, in “High Resolution X-ray Spectroscopy with XMM-Newton and Chandra”, Ed. G. Branduardi-Raymont, E34
- Rasmussen, A., et al. 2007, ApJ, 656, 129
- Rauch, M., et al. 1998, ApJ, 489, 1
- Raymond, J. C. & Smith, B. W. 1977, ApJS, 35, 419
- Roncarelli, M., et al. 2006, MNRAS, 368, 74
- Salpeter E. E., 1955, ApJ, 121, 161
- Schaye, J., et al. 2010, MNRAS, 402, 1536
- Sembach, K. R., et al. 2003, ApJS, 146, 165
- Simcoe, R. A., et al. 2006, ApJ, 637, 648
- Smith, R. K., et al. 2001, ApJ, 556, L91

- Snowden, S. L., et al. 1994, ApJ, 424, 714
- Snowden, S. L., et al. 1997, ApJ, 485, 125
- Soltan, A. M., Freyberg, M. J., Trümper, J. 2001, A&A, 378, 735
- Spergel, D. N., et al. 2007, ApJS, 170, 377
- Springel V., White M., & Hernquist L., 2001, ApJ, 549, 681
- Springel V., & Hernquist L., 2003, MNRAS, 339, 289
- Springel V., 2005, MNRAS, 364, 1105
- Tornatore, L., et al. 2009, MNRAS, in press
- Tripp, T. M., et al., 2008, ApJS, 177, 39
- Ursino, E. & Galeazzi, M. 2006, ApJ, 652, 1085
- Weinberg, D. H., A&A, 482, L29 Miralda-Escudé, J., Hernquist, L., & Katz, N. 1997, ApJ, 490, 564
- Werner, N., et al. 2008,
- Wiersma, R. P. C., Schaye, J., & Smith, B. D. 2009a, MNRAS, 393, 99
- Wiersma, R. P. C., et al. 2009b, MNRAS, 399, 574
- Williams, R. J. et al. 2005, ApJ, 631, 856
- Williams, R. J., Mathur, S., & Nicastro, F. 2006, ApJ, 645, 179
- Williams, R. J. et al. 2007, ApJ, 665, 247
- Yoshida, N., Furlanetto, S. R., & Hernquist, L., 2005, ApJ, 618, L91
- Yoshikawa, K., et al. 2003, PASJ, 55, 879
- Yoshikawa, K. & Sasaki, S., 2006, PASJ, 58, 641

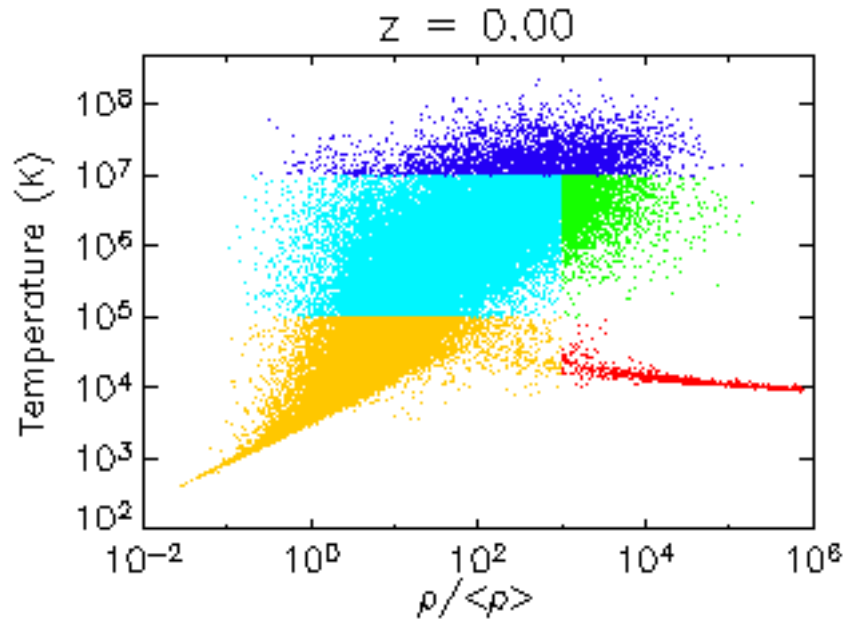


Fig. 1.— Phase diagram of the gas in the temperature-density space. Star formation is in *red*, the cold diffuse gas is in *yellow*, the WHIM is in *light blue*, groups of galaxies are in *green*, and galaxy clusters are in *blue*.

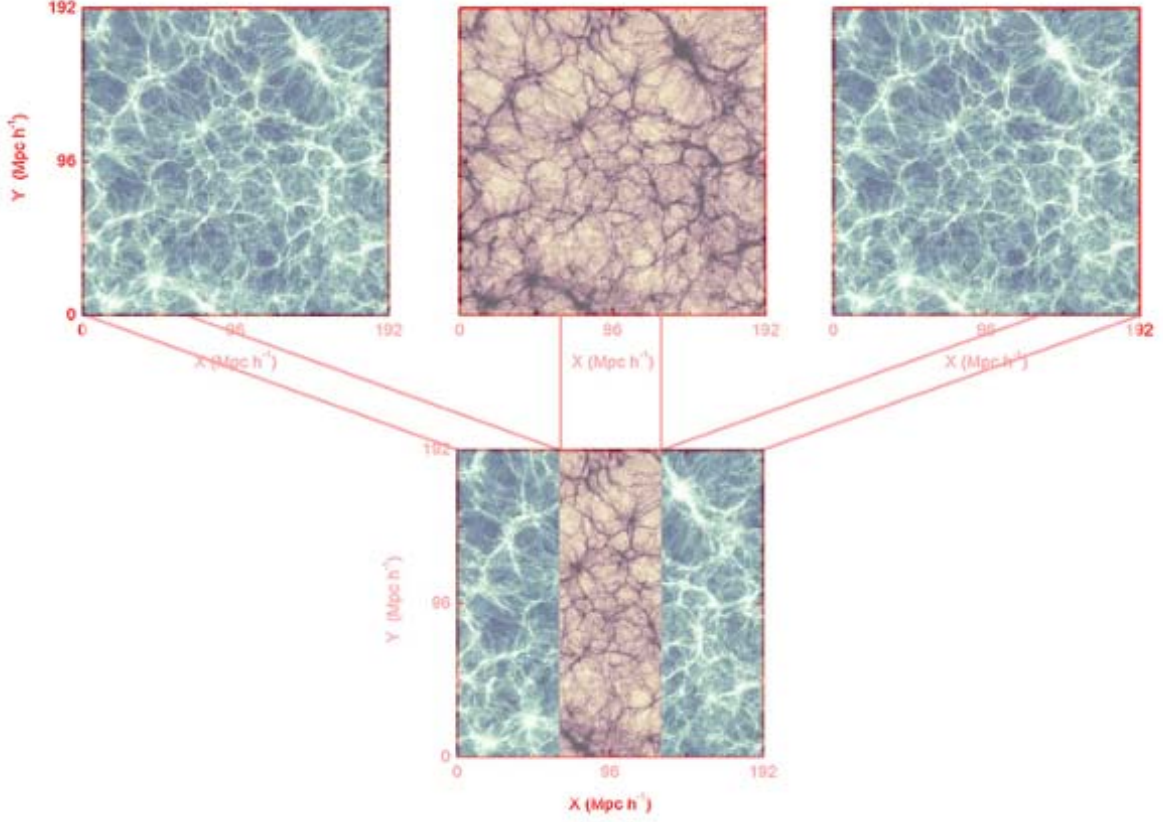


Fig. 2.— The program has redshift intervals too small to contain a full snapshot. Three slices of consecutive snapshots are added to form a cube for the simulation. The numbers are the redshifts of the snapshots used. The figure is elaborated from the map of gas density of Fig. 1 in Borgani et al. (2004). The color scale is in arbitrary units as the figure is meant only for describing the procedure.

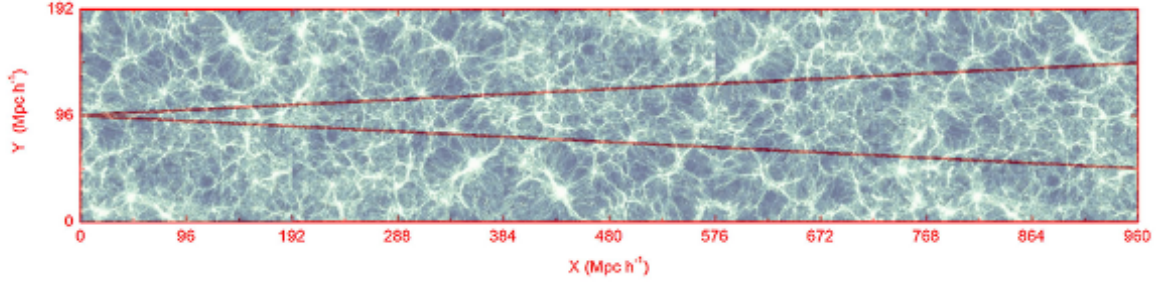


Fig. 3.— Piling up the boxes from Borgani model, the program creates a simulated light cone. Particles inside the field of view (defined by the red lines) are selected to simulate the X-ray emission. The figure includes the first five boxes (discontinuity at the boundaries are visible), spanning the redshift interval $0 - \sim 0.3$. The color scale is in arbitrary units as the figure is meant only for describing the procedure.

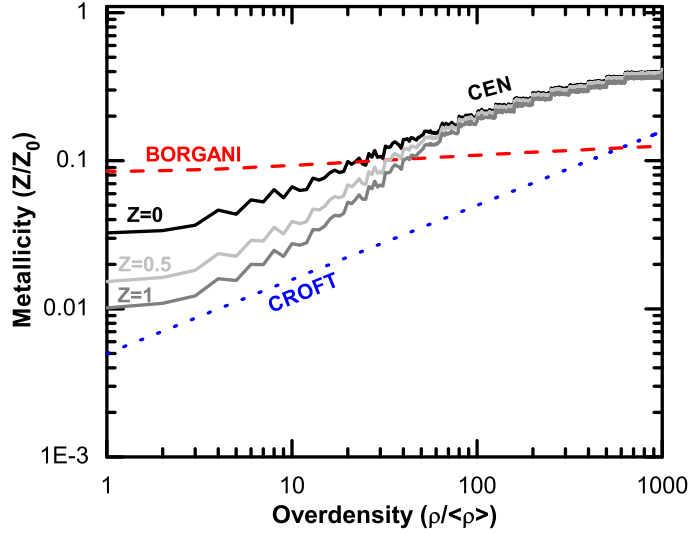


Fig. 4.— Average metallicity as a function of density for the four different models used in this paper. The Borgani model (*red dashed*) comes directly from the hydrodynamic simulation used in this paper Borgani et al. (2004). The Croft model (*blue dotted*) is derived from Croft et al. (2001). The Scatter and Cen models (*black solid*) come from a random selection based on the distribution function from Cen cubes Cen & Ostriker (1999a). The two models are identical at $z=0$, but the Cen model includes a dependence on redshift following Cen & Ostriker (1999b); the average metallicities for the Cen model at $z=0.5$, and $z=1$ is also shown (*gray solid*).

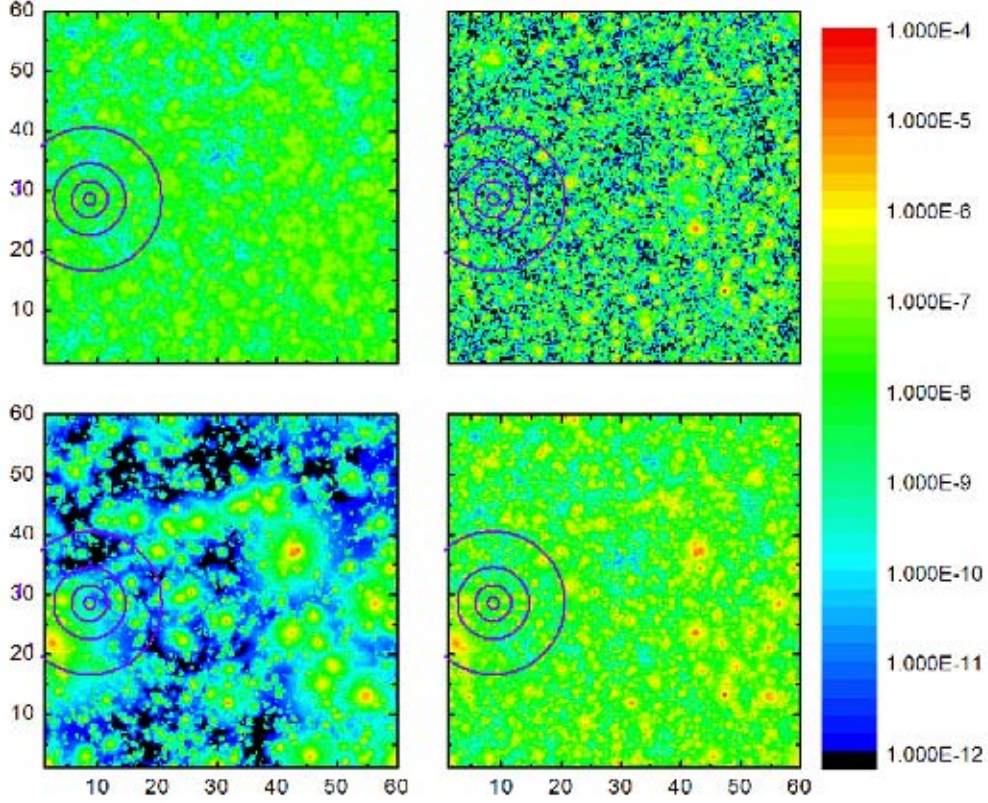


Fig. 5.— Simulations of the emitted X-rays from the WHIM (*top left*), the dense WHIM (*top right*), the hot gas (*bottom left*), and the total gas (*bottom right*) in the full line of sight, up to $z = 2$. The circles represent different fields of view with radii 1', 3', 6', and 12'. The map has a FOV of $1^\circ \times 1^\circ$ and 256×256 pixels (resolution of $14''$) in the energy range 380–950 eV, and uses the Croft metallicity model. Units for the color bar are $\text{photons cm}^{-2} \text{s}^{-1}$.

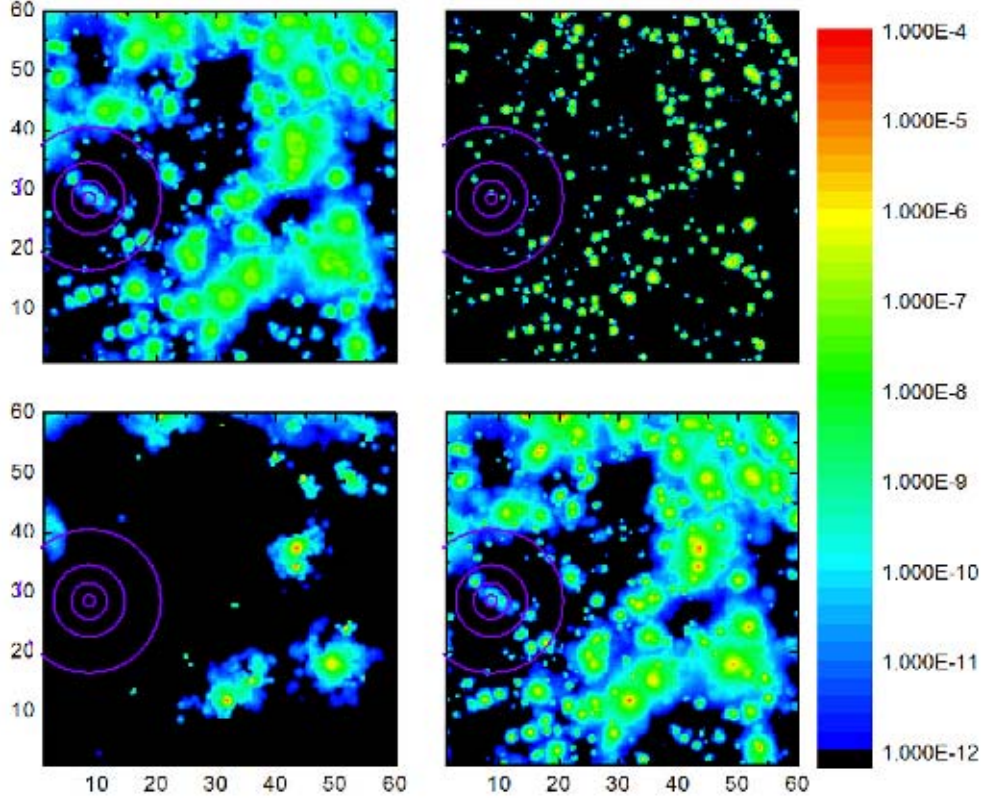


Fig. 6.— Simulations of the emitted X-rays from the WHIM (*top left*), the dense WHIM (*top right*), the hot gas (*bottom left*), and the total gas (*bottom right*) from slice # 4 ($z \sim 0.25$, thickness $192 \text{ h}^{-1} \text{ Mpc}$) of the same simulation of Fig. 6. The circles represent different fields of view with radii $1'$, $3'$, $6'$, and $12'$. The map has a FOV of $1^\circ \times 1^\circ$ and 256×256 pixels (resolution of $14''$) in the energy range $380 - 950 \text{ eV}$, and uses the Croft metallicity model. Units for the color bar are $\text{photons cm}^{-2} \text{ s}^{-1}$.

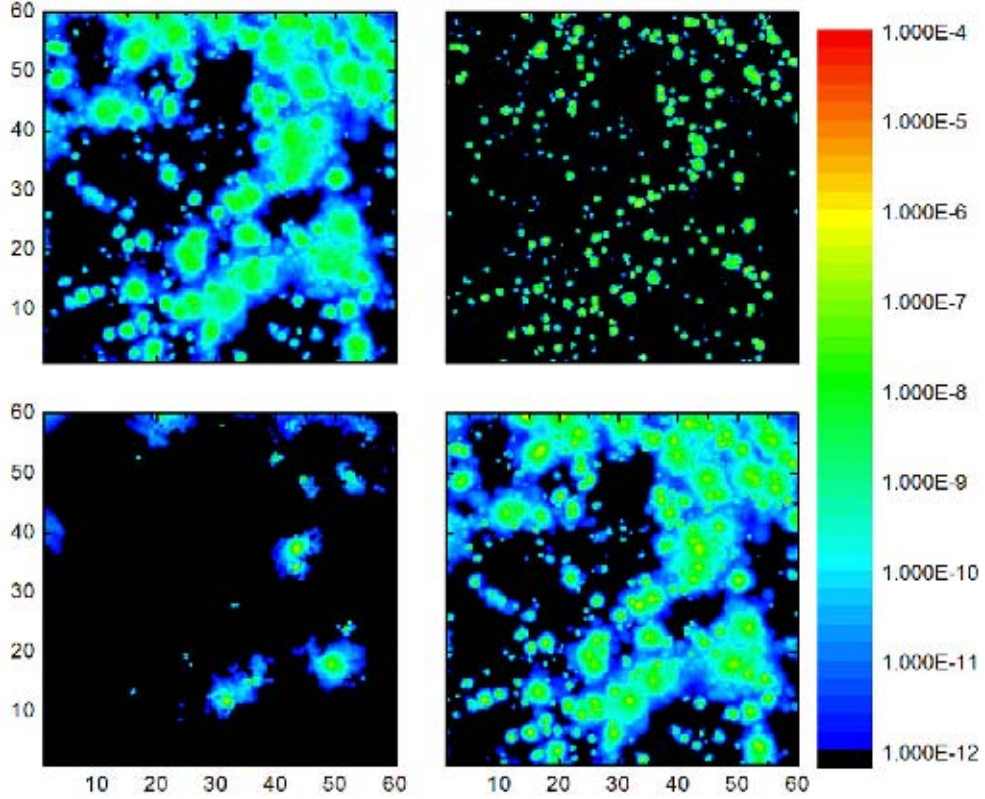


Fig. 7.— Simulations of the emitted X-rays from the WHIM (*top*), the dense WHIM (*center*), and the hot gas (*bottom*) in the same field of view and redshift range of the simulation of Fig. 6, the energy range corresponds to the O VII (561 – 574 eV) band redshifted at $z=0.25$. The map has a FOV of $1^\circ \times 1^\circ$ and 256×256 pixels (resolution of $14''$) and uses the Croft metallicity model. Units for the color bar are photons $\text{cm}^{-2} \text{s}^{-1}$.

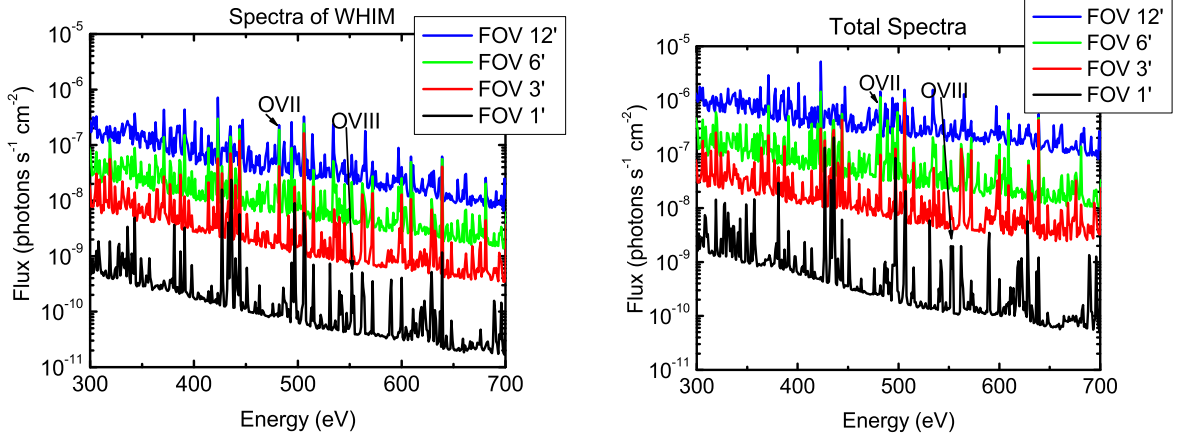


Fig. 8.— Spectra extracted from the pointing shown in Fig. 6 with radii 1', 3', 6', and 12', using data for the WHIM only (*left*) and for the sum of WHIM, dense WHIM, and ICM (*right*).

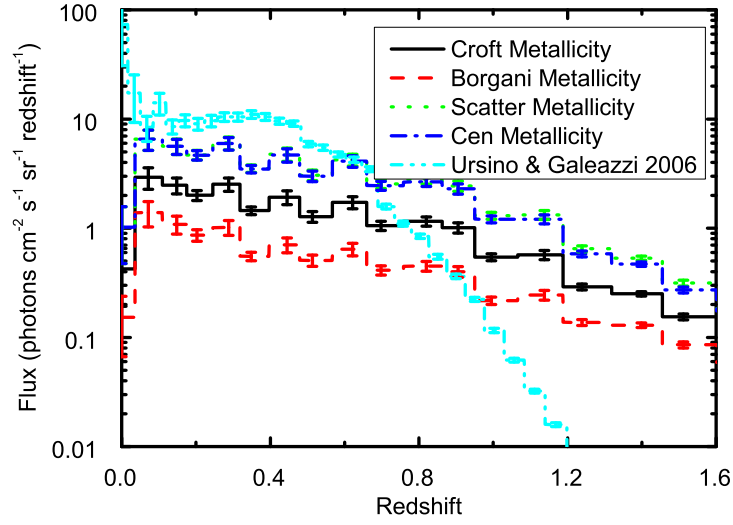


Fig. 9.— Expected surface brightness in the energy range 0.380-0.950 keV due to the WHIM as a function of redshift depending on the metal model. Borgani metallicity is *dashed red*, Croft metallicity is *solid black*, Scatter metallicity is *dotted green*, and Cen metallicity is *dot-dashed blue*. For comparison, the results of our previous work Ursino & Galeazzi (2006) are in *double dot-dashed light blue*.

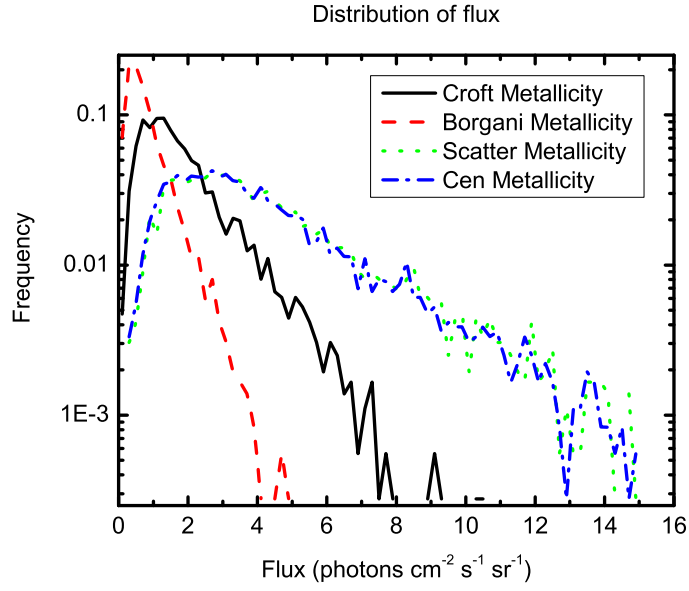


Fig. 10.— Distribution function of surface brightness of the WHIM for simulations with FOV of 3' for the four metallicity models considered. Borgani metallicity is *dashed red*, Croft metallicity is *solid black*, Scatter metallicity is *dotted green*, and Cen metallicity is *dot-dashed blue*.

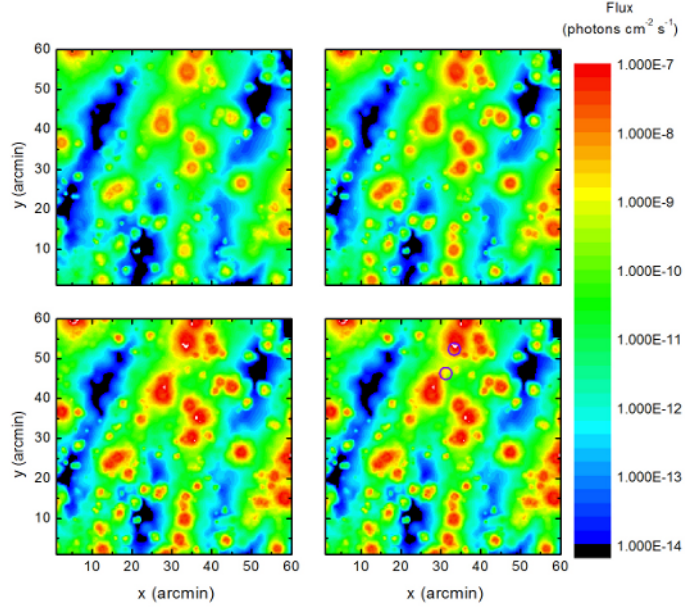


Fig. 11.— Simulated WHIM maps at redshift $z = 0.13 - 0.20$ with the Borgani metallicity model (*top left*), the Croft model (*top right*), the Scatter model (*bottom left*), and the Cen model (*bottom right*). The black circles in the bottom right image are centered on a dark and a bright region used to extract the spectra in Fig. 6. The maps have a FOV of $1^\circ \times 1^\circ$ and 256×256 pixels (resolution of $14''$) in the energy range $380 - 950$ eV.

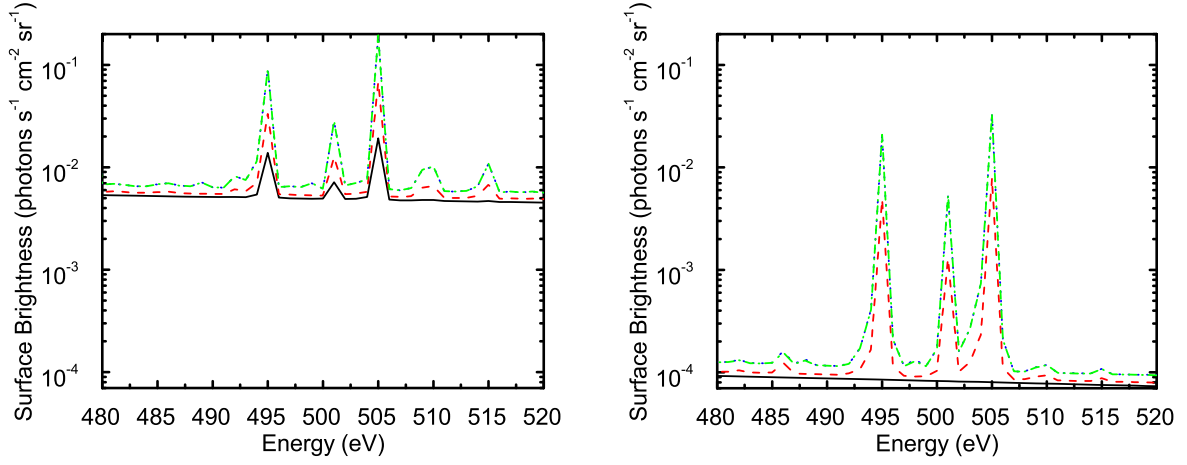


Fig. 12.— Zoom in the 480 – 520 eV of the simulated emission spectra from the selected dark and bright WHIM regions in the bottom right map of Fig. 6. The lines shown correspond to redshifted O VII triplet. The spectra are relative to simulations with the Borgani metallicity model (*solid black line*), the Croft model (*dashed red line*), the Scatter model (*dotted green line*), and the Cen model (*dot-dashed blue line*).

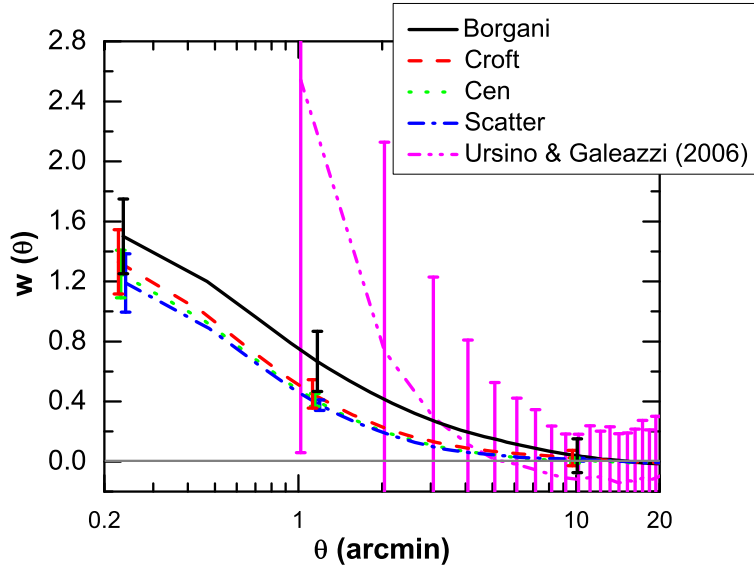


Fig. 13.— Average angular autocorrelation function of the WHIM for the Borgani (*solid black*), Croft (*dashed red*), Cen (*dotted green*), and Scatter (*dot-dashed blue*) metallicity models compared with our previous work (*double dot-dashed purple*). The error bars represent the cosmic variance for each set of maps.

Table 1. Average WHIM metallicity, surface brightness (SF) in the energy range 0.380-0.950 keV (in units of photons cm⁻² s⁻¹ sr⁻¹), and predicted flux in the RASS *R4* and *R5* bands in units of 10⁻⁶ photons s⁻¹ arcmin⁻² (the default RASS units). The metallicity is calculated at redshift 0.

Model	$\frac{Z}{Z_{\odot}}$	SF	RASS R4 flux	RASS R5 flux
Borgani	0.103	0.77 ± 0.04	1.2 ± 0.2	1.3 ± 0.3
Croft	0.043	1.84 ± 0.08	3.4 ± 0.6	3.1 ± 1.7
Scatter	0.158	4.3 ± 0.2	8.4 ± 1.5	7.2 ± 1.7
Cen	0.158	4.2 ± 0.2	8.2 ± 1.6	7.1 ± 1.7